INSTRUCTIONAL LABORATORIES AND DEMONSTRATIONS | APRIL 01 2023

An economical smoke chamber and light-sheet microscope system for experiments in fluid dynamics and electrostatics

VIDEO

Karl D. Stephan

Am. J. Phys. 91, 316 (2023)
https://doi.org/10.1119/5.0122766

John Essick, *Editor*
Department of Physics, Reed College, Portland, OR 97202

Articles in this section deal with new ideas and techniques for instructional laboratory experiments, for demonstrations, and for equipment that can be used in either. Although these facets of instruction also appear in regular articles, this section is for papers that primarily focus on equipment, materials, and how they are used in instruction. Manuscripts should be submitted using the web-based system that can be accessed via the American Journal of Physics home page, ajp.aapt.org, and will be forwarded to the IL&D editor for consideration.

An economical smoke chamber and light-sheet microscope system for experiments in fluid dynamics and electrostatics

Karl D. Stephan[a)]
Ingram School of Engineering, Texas State University, San Marcos, Texas 78666

(Received 25 August 2022; accepted 9 January 2023)

A smoke chamber and light-sheet video microscope setup is relatively easy to construct and provides opportunities for undergraduates to participate in a variety of advanced experiments, including the demonstration of Brownian motion and the interaction of induced electrostatic dipoles in aerosol particle agglomeration. We present results of these experiments along with information to allow replication of the setup in undergraduate physics laboratories. A theoretical model of the rate of aerosol agglomeration of long dipole chains as a function of electric field agrees with experiments at field strengths up to 200 kV m^{-1}.
https://doi.org/10.1119/5.0122766

I. INTRODUCTION

Once students have mastered the basics of electromagnetics and statistical physics, they can tackle more complex interdisciplinary experiments that combine familiar concepts with new ones from more advanced areas of physics. Phenomena such as Brownian motion and the related concepts of diffusion and fluid-dynamic drag can be fruitfully studied in a variety of experiments ranging from simple video capture of microspheres in purified water[1,2] to more complex systems involving quadrupole ion traps.[3] While these experiments can be elegant and pedagogically rewarding, devoting time and resources to build a system that allows only one experiment is not always the best investment. A better approach for laboratories with limited resources is to develop an experimental hardware base that can be used to demonstrate an expandable variety of concepts covering a number of topics.

In this paper, we present a system that allows the microscopic study of aerosol particles in a variety of circumstances that illustrate concepts in fluid dynamics, electrostatics, and aerosol science. The system uses a "light-sheet" microscope.[4] Originally developed for imaging colloidal particles smaller than the limiting resolution of an optical system, a light-sheet microscope produces a thin, flat beam of light perpendicular to the line of sight of the imaging objective. Objects in the sheet's volume appear as bright spots against a dark background, and the resulting high-contrast images are easily processed by automated imaging software. After the original concept was described in the early 1900s, some of the earliest aerosol-science research into the nature and concentration of smoke particles used the light-sheet technique.[5] We have developed a simplified form of this setup that can demonstrate a wide variety of phenomena in the areas of fluid dynamics, electrostatics, and aerosol science.

The most costly item in the setup is a video-equipped microscope. Many of the system's other components can be fabricated from scratch if necessary or procured from hardware stores. The genesis of this system came about during COVID-19, when my university shut down all on-campus lab-based research and student involvement for the better part of 2020, and I set up a small laboratory at my house to pursue some ideas on my own in aerosol interactions with electric fields. By necessity, no students were involved at the time. However, the fact that the system was built by one person (except for the occasional assistance of my wife) with almost no immediate outlay of significant funds indicates that it should be easy to duplicate elsewhere. The equipment needed should be found in any reasonably well-equipped undergraduate physics lab: a microscope equipped with a video recording system, some simple optics, and an optional high-voltage power supply and vacuum pump.

With the aid of free image-analysis software, students can perform experiments demonstrating Brownian motion and the agglomeration of smoke particles in electric fields, among others.

Following a description of the hardware setup, we describe these experiments and provide samples of experimental results.

II. EXPERIMENTAL MATERIALS AND METHODS

To produce aerosol particles of fairly consistent number density and composition is not an easy process in general.

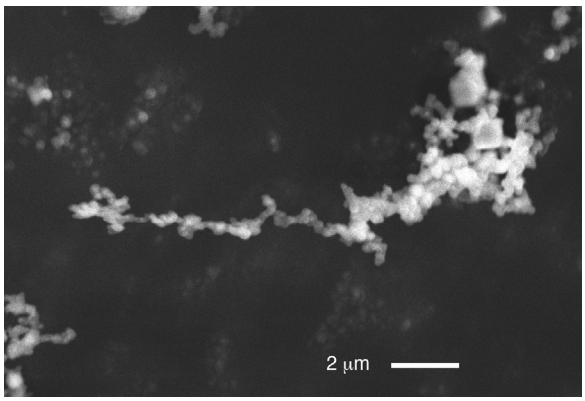

Fig. 1. Long particle chain of MgO monomers (cubic crystals).

After several unsuccessful tries using ready-made powders, we found that MgO smoke particles produced by combustion of strips of elemental magnesium in ambient air were the best source to use in terms of consistency and reliability. Regarding the safety of this process, burning magnesium should be enclosed in a fireproof enclosure and should not be viewed at close range without eye protection. MgO smoke is non-toxic, and the oxide is a component of many commonly used refractory materials. If release of the small amount of MgO smoke created in this experiment is a concern, a vacuum cleaner equipped with a HEPA filter can be used to capture the smoke exhausted from the system to keep it from entering the laboratory environment.

MgO smoke consists primarily of small nearly perfect cubes (~60–100 nm on a side) intermixed with less common larger cubes. The surface energy of MgO is about 1.1 J m^{-2},[6] comparable to elemental Si, and the van der Waals forces between small cubic crystals of MgO are correspondingly large. Consequently, isolated cubic crystals are almost never found in samples of MgO smoke obtained for microscopic analysis. SEM examination shows MgO smoke particles consist of interlocked chains (Fig. 1) and more complex formations (Fig. 2). These formations are quite rugged, in the sense that while they will flex and change shape under aerodynamic or electrostatic stress, it takes a comparatively large force to rupture a chain.

Electrically, MgO is a good but not perfect insulator. In addition, most materials in ambient air with relative humidity (RH) above about 20% acquire at least a monolayer of water molecules. This monolayer can produce a nonzero electrical conductivity for these aggregates. Crystalline MgO has an isotropic relative permittivity of 9.9,[7] so both isolated particles and aggregates of particles will polarize significantly in an electric field. In addition to the usual dielectric polarization induced by an externally applied field, aerosols can acquire a net charge from collisions with ions of either sign. Combustion in air usually leaves a slight net charge on aerosol particles, but in our specific experiments, this charge is equal to or less than the expected Boltzmann-distributed bipolar equilibrium charge,[8] with a slight bias toward positive charge of about one electron per smoke particle, whose average radius of gyration is about 10 μm.

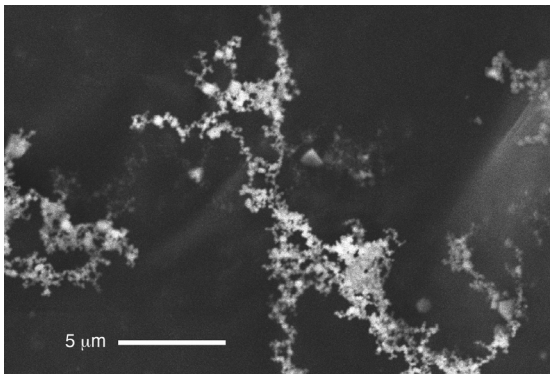

Fig. 2. Complex of MgO particles showing multiply connected structures.

The experimental setup used is a modified "ultramicroscope" or light-sheet system, in which a thin slice of an aerosol is illuminated by a beam of light that is perpendicular to the imaging microscope's line of sight. Figure 3 shows a photograph of the setup, including the two microscope objectives. The objective on the right side of the photo creates the light sheet as a thin horizontal strip with its narrowest portion directly beneath the imaging-microscope objective. The light sheet is centered between the two electrodes, which were parallel discs set to a spacing of 4.2 mm in most of the experiments, as shown in the drawings of Fig. 4. With a 1.5-kV DC power supply, this spacing allowed the creation of fields up to about 350 kV m^{-1}. The optional high-voltage power supply used should have an accuracy of about ±2%. The current drawn is only on the order of μA, so a current-limiting resistor or other means for limiting the current to a safe value can be placed in the power-supply circuit.

The 25 cm^3 smoke chamber was made of transparent acrylic-plastic sheet and enclosed on all sides. To prevent any permanent charge on the plastic sheet surface from interfering with the experiment, the inside of the chamber was painted with grounded conductive paint (MG Chemicals 838AR Total Ground) except for ~2 cm-diameter circular patches masked off to allow the light source to enter and the microscope to view the smoke, along with patches near the electrode entry points to prevent shorting.

The light source optics were fabricated using an Eisco Labs optical bench and attachment kit, available from

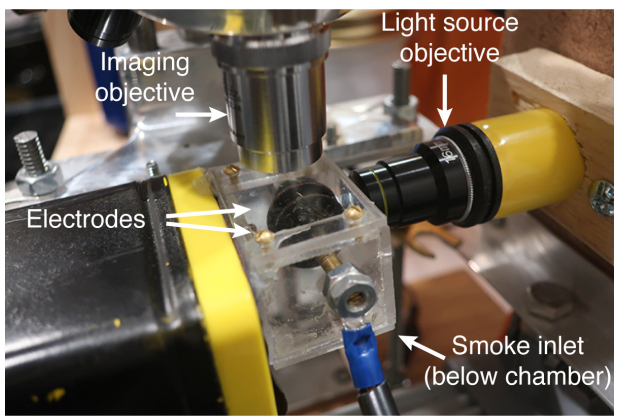

Fig. 3. Photo of smoke chamber used for studies of smoke particle chains. The light sheet enters from the light-source objective on the right, is focused to a thin sheet below the imaging objective, and exits into the black metal enclosure on the left. The round black-painted electrodes have a 4.2-mm gap between them. Smoke enters through a small tube at the bottom of the chamber below the light-source objective. The chamber is screw-mounted to a yellow plastic panel that snaps into the black metal enclosure on the left for convenient mounting and demounting. This photo was taken prior to painting the interior of the chamber with black conductive paint to reduce effects of fixed charges in the plastic walls.

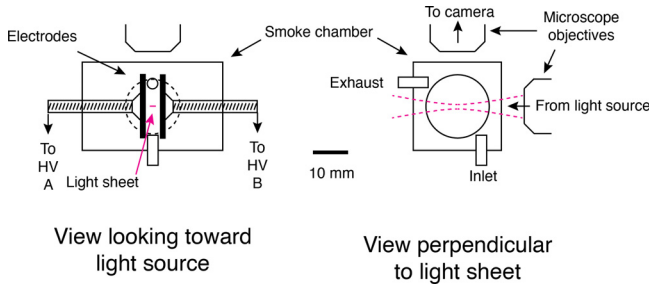

Fig. 4. Drawings of smoke chamber viewing toward light source (left) and perpendicular to light source (right). Contour of light sheet is shown in red.

sources such as hbarsci.com for less than $200, plus a microscope objective lens. In some later experiments, a variable-focal-length InfiniProbe microscope (model S-50) was used, but a standard microscope with a turret of various fixed-focal-length objectives can be used as well. Instead of the incandescent lamp source provided with the bench kit, whose infrared radiation might cause undesirable heating and convection within the smoke chamber, we substituted an intense LED lamp obtained from a low-voltage garden light of the type obtainable from hardware stores, operating from 12 VDC. The slit and 50-mm positive-focal-length lens provided with the Eisco Labs kit combined with a 16-mm focal-length microscope objective to make a light sheet whose transverse dimensions were approximately 2.7 mm wide by 540 μm deep at the focal point of the camera objective. More sophisticated light-sheet optics can use a laser source and a cylindrical lens instead of a slit to produce a more intense sheet,[4] but the simpler system we used proved entirely adequate for the experiments we performed.

Smoke was generated in a 750 cm^3 glass-walled combustion chamber by igniting a magnesium strip weighing approximately 22 mg with a low-voltage NiCr heater wire in direct contact with the strip. The combustion chamber was fabricated from a one-quart canning jar with copper tubing soldered to the steel lid and insulated bushings connecting to the replaceable heater wire, which was procured from a hair dryer. Commercial sources of laboratory glass containers and NiCr wire can be used as well.

At first, smoke was injected with a manually operated piston in a cylinder adapted from a basketball inflator pump, but this method did not allow precise control of the injection velocity. For some experiments, precise control is not needed, but for the dipole-interaction experiments described below, a fairly uniform smoke density improves repeatability and was obtained using plastic valves and tubing from a retail aquarium supply store.

After igniting a Mg strip to produce smoke, a sample of the resulting smoke was then withdrawn during combustion into a small ($\sim$400 cm^3) latex party balloon by means of a vacuum system. Referring to Fig. 5, the sampling balloon was initially connected to the combustion chamber in position A. Valve V_2 was closed, V_1 was opened, and the vacuum reservoir evacuated to an absolute pressure of about 50 kPa. V_1 was then closed, the Mg strip was ignited with an electrical heater (not shown), and 60 s was allowed to elapse in order for the largest smoke particles to precipitate out of the smoke in the combustion chamber and for the remainder of the smoke to homogenize by convection.

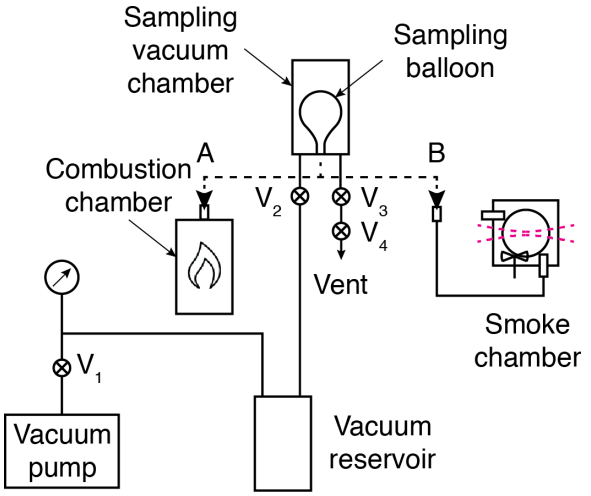

Fig. 5. Smoke sampling and injection system for constant-flow injection of smoke into chamber.

The smoke in the chamber was then sampled by opening V_2, which inflated the balloon so that it withdrew about 300 cc of smoke from the combustion chamber. Then, V_2 was closed, leaving the balloon inflated with smoke inside the sampling vacuum chamber, which was under a partial vacuum.

To inject smoke into the smoke chamber for examination, the sampling balloon assembly was removed from A and connected to position B, which led through a short piece of tubing to the smoke chamber. Valve V_4 had previously been adjusted to leak only enough airflow into the sampling vacuum chamber to allow the balloon to deflate in 65 s. To inject smoke into the smoke chamber, V_3 was opened to allow this flow rate determined by V_4 to gradually inject smoke into the chamber. The small controllable leak provided by V_4, thus, allowed a smooth, constant rate of smoke injection into the observation chamber, driven by the elasticity of the balloon.

With electrodes spaced 4.2 mm apart, the smoke moved by laminar flow in a primarily horizontal direction from the inlet port to the exhaust port. Once enough fresh smoke entered the smoke chamber to ensure that any previous smoke particles had been effectively purged from view, valve V_3 was closed, stopping the injection of smoke and allowing experiments to proceed.

It was not possible to fabricate the smoke chamber to allow hermetic sealing, which would have caused problems in any case by making the pressure in the chamber above atmospheric. Instead, the end opposite the light source was vented to the atmosphere. While the chamber walls isolate the smoke inside from most exterior air currents, the fact that the chamber is open to atmospheric pressure allows infrasound pressure and velocity variations to enter the chamber. For example, moving one's hand near the chamber can cause visible motion of the smoke particles, as will the opening of a door in the room. So, some care is needed in choosing an acoustically quiet environment for the experiments.

III. EXPERIMENTS

A. Brownian motion

The theory of Brownian motion is well-developed, having been established by Einstein in 1905.[9] His theory is regarded

as providing some of the most concrete evidence then available for the existence of atoms and molecules, and experiments involving Brownian motion can reinforce key concepts in an undergraduate physics curriculum.

Brownian motion is a diffusion process. The drag force F_D is described by Stokes's law

$$F_D = 3\pi\eta v d, \tag{1}$$

where η is the fluid dynamic viscosity, v is the velocity, and d is the particle diameter (the particle is assumed to be spherical).[8] Stokes's law is valid for particles larger than about 1 μm in low-velocity flow, which covers most of the particles in these experiments.

For such particles, the diffusion coefficient D is given by the Stokes–Einstein relation

$$D = \frac{k_B T}{3\pi\eta d} \tag{2}$$

in which k_B = Boltzmann's constant. Einstein's theory then predicts that in the absence of any net fluid flow, the movement of a particle in one dimension (say Δx) over a total elapsed time Δt, if measured many times, will form an ensemble with a Gaussian distribution whose variance σ^2 is given by

$$\sigma^2 = 2D\Delta t. \tag{3}$$

The experiment consists in tracking a large number of smoke particles using the TrackMate plugin of the free software package Fiji/ImageJ (available at https://imagej.net/software/fiji/downloads). Details of the tracking and analysis procedures are given in the supplementary material.[10]

Ideally, there would be no net motion of the particles (zeroth moment), but in an unsealed chamber this is almost impossible to achieve due to differential room heating, drafts, etc. However, the motion in a direction perpendicular to the net flow is due only to Brownian diffusion.[11] Mathematical rotation of the original (x, y) coordinate system through an angle θ to yield the rotated system (x', y') always produces an angle θ_0 for which the particle motions in one of the rotated coordinates (x' or y') have no average motion (zeroth moment of zero). The data from that rotated coordinate with zero net flow in the rotated coordinate system can then be used to fit a Gaussian and derive a value for D.

Figure 6 shows the results from one such experiment that tracked 355 particles over an average time of $\Delta t = 0.35$ s per particle. The data were extracted from a video with a 29.97 fps frame rate lasting a total time of 6.7 s. The Gaussian best-fit curve in a least-square sense has a standard deviation $\sigma = 0.91$ μm, which combined with the average Δt in Eq. (3) yields a diffusion constant $D = 1.183 \times 10^{-12}\,\mathrm{m^2\ s^{-1}}$. Equation (2) shows that the average effective diameter of particles with this diffusion constant at $T = 300$ K is 20.5 μm, which is consistent with other measurements we have made of the average particle diameter.

Strictly speaking, with a sample of particles whose diameters are Gaussian-distributed about a mean diameter d_0, the correct way to analyze the situation is to divide the sample into small cohorts of same-size particles, derive the appropriate D and Gaussian distribution in space for that cohort, and sum up (or numerically integrate) the contributions of each cohort. For a size distribution that is narrowly peaked around d_0, as ours appears to be, the result of the more complex analysis will be indistinguishable from treating the sample as if it were monodisperse (all particles with d_0).

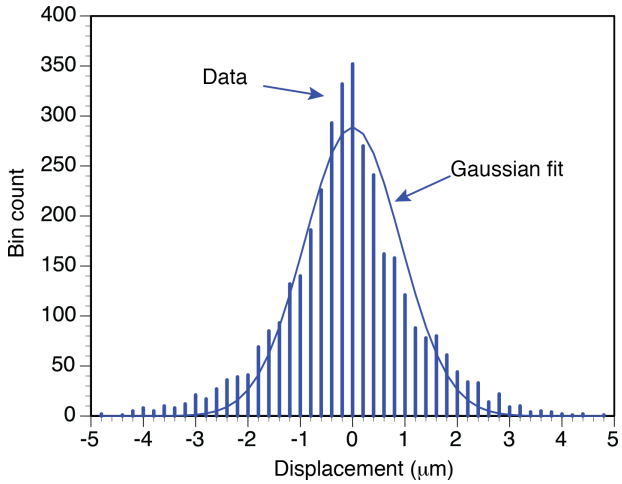

Fig. 6. Experimental Brownian-motion data from 355 particles tracked during an average tracking time of 0.35 s at room temperature. Each displacement is measured for a one-frame interval of 1/29.97 = 33.367 ms. The least-squares-fit Gaussian shown has a standard deviation $\sigma = 0.91$ μm, which implies an average particle size of about 20 μm.

This experiment requires only a few seconds' worth of video data, and the analysis process can be completed in less than 30 min, not counting the time required to generate graphs.

B. Dipole–dipole interactions and particle agglomeration

As mentioned above and confirmed by Brownian-motion experiments, the average diameter of the MgO smoke particles as generated by combustion is about 20 μm, although there are a few isolated longer chains of MgO crystals initially. However, when an electric field is applied to the smoke, the particles acquire induced dipole moments and begin to agglomerate in long chains. Charged particles also begin to precipitate onto the electrodes, although as we mentioned earlier, the charges on most particles are small and precipitation becomes significant only at very high fields, exceeding 200 kV m^{-1}.

What this means is that for a field of view covering 1–2 mm, many particles remain visible for several video frames (50–200 ms) as they fall through the focal depth of the imaging optics and can be studied and analyzed using Fiji/ImageJ in a variety of ways. We chose to demonstrate this capability of the setup by studying the degree to which long particle chains form as a function of electric field intensity.

The procedure followed was to inject a fresh (<3 min old) sample of MgO smoke into the chamber, allow it to reach approximately zero average velocity, and then apply a calibrated electric field for a 20 s period. All frames during the application of the field were then analyzed for long chains by means of Fiji/ImageJ.

ImageJ defines particle circularity C_P as

$$C_P = 4\pi \frac{(\mathrm{Area})}{(\mathrm{Perimeter})^2}, \tag{4}$$

where the area and perimeter are calculated by ImageJ algorithms. A perfectly circular particle has a circularity of 1.0, while an ellipse has a circularity <1. We found that

particles with circularity <0.3 were almost always long particle chains of the type formed by electric fields. In the absence of an electric field, the fraction of particles in all zero-field experiments with circularity <0.3 was 6.3×10^{-6}, a fraction far less than the percentage of chains found under the influence of electric fields. We, therefore, chose to define a long particle chain as one with circularity <0.3, to discriminate between original particles and those that have formed into long chains under the influence of the electric field.

We give a detailed analysis of the forces between dipoles and how it influences the agglomeration of long chains in the supplementary material.[10] What may be more appealing to undergraduate students than the mathematical details of dipole–dipole interaction is seeing two or more dipoles approach and connect with each other, and this type of event occurs many times during a typical series of runs. A sequence of stills from one video during which a field of $95\,\mathrm{kV\,m^{-1}}$ was present in the light-sheet volume is shown in Figs. 7(a)–7(h). This sequence shows an enlarged section of the field of view in which a longer chain first joins a shorter chain to its upper left and then the combination attracts a third chain to its lower right. The dynamics of the attraction process are such that chains with ends that are closer than about 100–200 μm of each other are likely to join, and the joining process itself takes typically 50 ms or less.

Fiji/ImageJ calculates the perimeter of each particle, which for long chains is a good proxy for twice the chain length, as the width of chains formed by electric fields remains close to the original particle diameter of 10–20 μm. The data showing how particle perimeter varies with electric field can be presented in two ways, both of which we will now illustrate with examples.

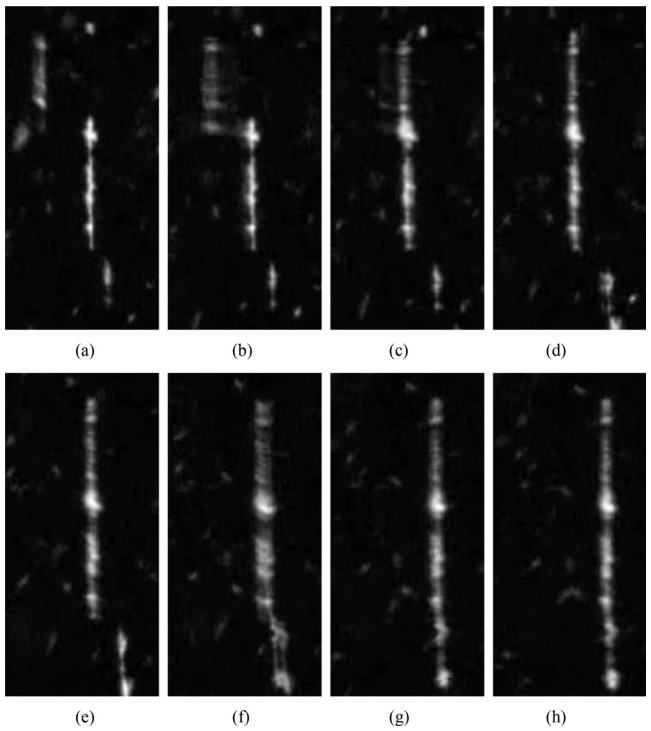

Fig. 7. Sequence of eight frames (a)–(h) (enlarged section of field of view) showing three separate chains merging into one about 450 μm long. Time interval between frames: 33.367 ms. Multimedia view: https://doi.org/10.1119/5.0122766.

Figure 8 shows a summary that shows every long particle chain (circularity < 0.3) detected in each of four trials using the following field strengths: 0, 47.6, 95.2, 119, 143, 190, 298, and $354\,\mathrm{kV\,m^{-1}}$. The x-axis is a frame number for each 20-s experimental run, ranging from 1 to 600. The y-axis is the perimeter of each particle counted by ImageJ.

As expected, very few (only four) chains appear in the 0-V plot, but fields as small as $47.6\,\mathrm{kV\,m^{-1}}$ give rise to substantially more chains. At $95.2\,\mathrm{kV\ m^{-1}}$, a trend toward larger chains showing up in later frames begins to emerge, and the density of chains increases. This trend is very clear in the $119\,\mathrm{kV\ m^{-1}}$ plot, which also shows how different four independent trials can be despite attempts to make the initial conditions similar. At $143\,\mathrm{kV\ m^{-1}}$, chain formation appears to be fairly evenly distributed throughout the length of the 20-s run, but at $190\,\mathrm{kV\ m^{-1}}$, a clear tendency for chain formation to cluster in the early part of the trial arises. This may not be so much that the rate of chain formation itself decreases, but at the higher fields, chains with nonzero net charge will move faster toward the oppositely charged electrode and precipitate out of the experimental volume. The effect of precipitation dominating over chain formation becomes very obvious in the 298 and $354\,\mathrm{kV\ m^{-1}}$ trials, in which most of the longest chains appear within a few seconds of the field turn-on time and then disappear due to precipitation to the electrodes.

Another significant measure is the average concentration of particle chains of any length vs the applied electric field, again for an experiment period of 20 s. Because the initial concentration from run to run is difficult to control (the average particle count in the field of view used for all 176 trials was 41.81 and the standard deviation was 26.12), the concentration of long chains is also expected to have a comparable spread. However again, a clear trend is visible in Fig. 9. The concentration of long chains rises by two orders of magnitude for fields as low as $50\,\mathrm{kV\ m^{-1}}$ and continues to rise up to a field of about $200\,\mathrm{kV\ m^{-1}}$. The number of chains counted declines at higher fields, though in an irregular fashion. The rate of chain formation begins to increase again at $354\,\mathrm{kV\ m^{-1}}$, but equipment limitations made this the highest field attainable with the boundary conditions and electrode gap chosen. As explained above, competition between chain formation and precipitation is at least partly responsible for the decline in chain concentration above $220\,\mathrm{kV\ m^{-1}}$. A theoretical explanation of this trend based on the general dynamic equation (GDE) proposed by Friedlander[12] is provided in the supplementary material,[10] and is the source of the theoretical GDE points shown in Fig. 9.Two interesting phenomena occur in longer chains when the field is turned off. A chain whose dipole moment has been acquired recently via dielectric polarization and which has not yet acquired a permanent dipole moment tends to go limp, acquiring a jagged but roughly linear shape dictated by the internal forces of the links making up the chain. However, chains that have existed long enough to allow mobile charges to create a semi-permanent dipole moment tend to collapse into a small lump, as the opposite charges on each end of the chain are no longer held in place by the external field, and suddenly attract each other instead. Figure 10 shows frames taken from such a collapse.

Finally, we will remark on the process that leads us to an estimate of the electrical resistance of long particle chains. Some long chains that are attracted to and make contact with an electrode are observed to remain stationary and intact,

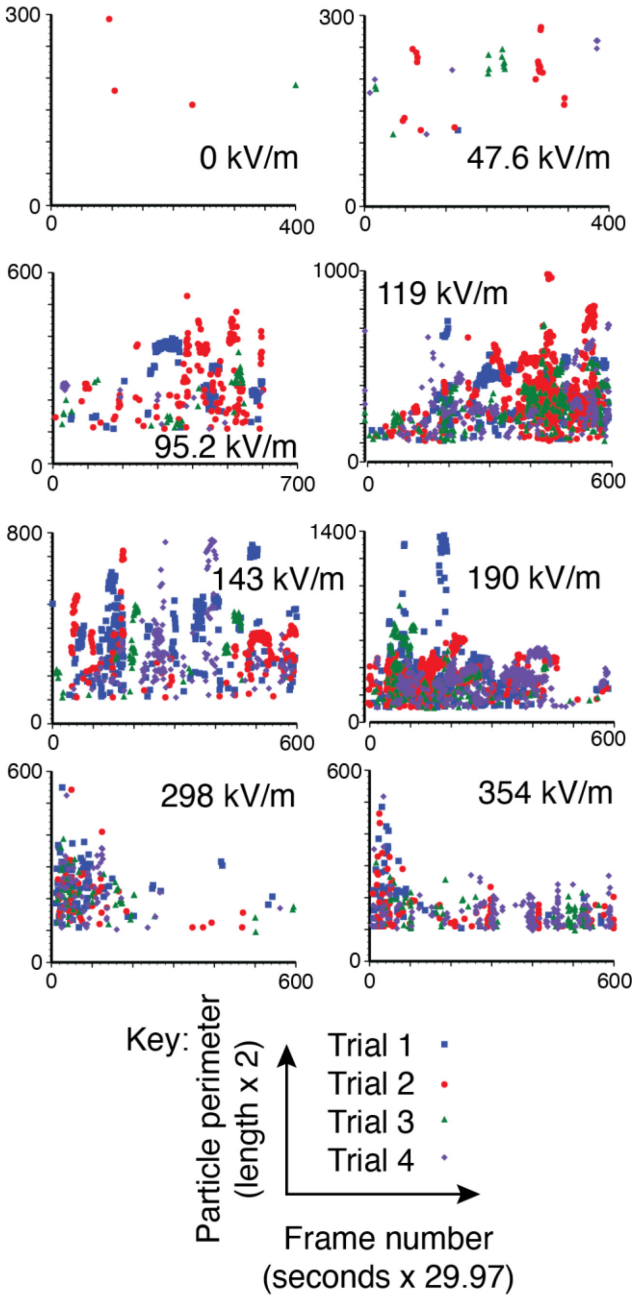

Fig. 8. Perimeters (in μm) of long particle chains vs video frame number for various electric fields in each of four independent trials.

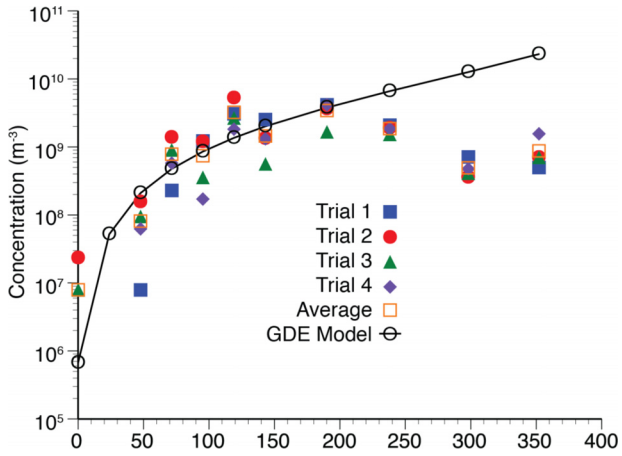

Fig. 9. Average experimental long-chain concentration for 20 s run for four independent trials at electric fields from 0 to 355 kV m^{-1}, together with simulation (hollow circles) from GDE model (for presentation of GDE analysis see the supplementary material (Ref. 10)).

perpendicular to the electrode plane, for a time on the order of seconds. A fraction of these then suddenly fly off the electrode and move across to the opposite electrode in less than one frame time (33.36 ms).

The explanation for this process is likely as follows. When the net charge on a long chain is sufficient to attract it to an electrode, the distribution of charge may be such that the chain remains intact upon contacting the electrode. While the chain's induced dipole moment will not be affected to first order by contact with the electrode, the net charge will be, because the chain begins to acquire charge of the same sign as the electrode by conduction once it contacts the electrode. This acquired charge is of opposite sign to the original net charge, and at a time when the overall force on the chain reverses sign, the chain detaches itself from the electrode. Once it is detached, the same-sign net charge acquired from the electrode furnishes a large repellent force that propels the chain across the gap to the other electrode.

An estimate of the chain's DC resistance can be made by estimating its capacitance C_C with respect to the electrode plane and equating its dwell time on the electrode to the time constant of an R–C lumped-element circuit. Sugiura[13] gives an expression for the capacitance of a monopole above a ground plane, which if the monopole is electrically short reduces to

$$C_C(pF) = \frac{55.6h}{\ln\left(\frac{h}{a}\right) - 1} \tag{5}$$

in which h is the monopole height in meters and a is the radius in meters. For a chain with $h = 1$ mm and $a = 10\,\mu$m, $C_C = 15.4$ fF. If the chain stays on the initially contacted electrode for $\tau = 3$ s, the equivalent lumped chain resistance R_C is approximately

$$R_C = \frac{\tau}{C_C} = \frac{3}{15.4 \cdot 10^{-15}} = 194\,\text{G}\Omega. \tag{6}$$

As the main contribution to conductivity is probably a thin film of water molecules adsorbed onto the surface of the MgO particles, this high level of resistance appears to be reasonable. It also indicates that the charge distribution on a long chain cannot be regarded as completely static but can change slowly under some conditions due to the non-zero conductivity of the chain. As mentioned previously, charge migration along a chain is probably the explanation for why some chains abruptly collapse into a small lump when the external field is removed.

While the large number of experimental runs presented here occupied most of a working day and required several days' worth of analytical effort, fewer runs could be performed with proportionally shorter analysis times. As for theoretical predictions, the simplest theory of which the author is aware dealing with agglomeration of aerosols is that of Smoluchowski,[14] which involves complex integral

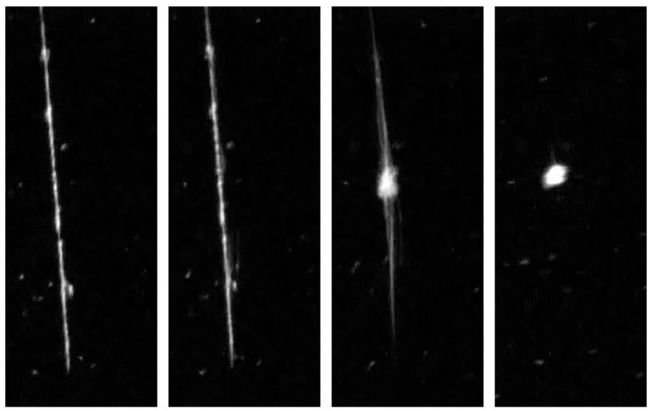

Fig. 10. Long particle chain (length ∼1 mm) collapsing after 95.2 kV m^{-1} field turned off at frame (a) (interval between frames: 33.367 ms). Multimedia view: https://doi.org/10.1119/5.0122766.

kernels and does not apply to inhomogeneous mixtures of particles of different size, although the theory has since been extended to such cases. In the supplementary material,[10] the GDE basis for the theoretical predictions is developed to support the theoretical curve in Fig. 9.

C. Other possible experiments

The experiments described above have been performed and verify that the results are acceptable for use in an undergraduate physics lab. Other possible experiments using the same setup and analysis software will now be described. While none of these have been performed in practice, they would require little or no additional equipment and only a modest analytical effort to develop.

1. Laminar flow

The narrow space between the electrodes (4.2 mm in the current setup) provides a good approximation to analyzing transverse fluid flow between infinite planes. The Reynolds number *Re* for such flow is given by

$$\mathrm{Re} = \frac{\rho L v}{\mu} \tag{7}$$

in which ρ is the density, L is the characteristic length (in this case, the space between the two planes), v is the fluid velocity, and μ is the dynamic viscosity. For a flow velocity less than about $v = 10$ m s^{-1}, the flow between the electrodes is laminar. Video particle tracking is a common technique used for imaging flow fields, and students can compare experimental flow fields measured with tracked particles using Fiji/ImageJ to the parabolic profile predicted by theory.[15]

2. Turbulent flow

Turbulence can be induced at least two ways in the setup: (1) by injecting smoke at a velocity high enough to exceed about 10 m s^{-1} in the interelectrode space or (2) by increasing the electrode spacing and applying a sufficiently high field. Beyond a certain limit of particle density, charge, and field, the smoke particles cease to behave as independent entities in an otherwise stationary medium and begin to influence each other, an effect dealt with by Fuchs[16] which he terms the hydrodynamic interaction of aerosol particles. While analysis and calculations of turbulent flow are notoriously complex, a qualitative demonstration is easy to produce with this setup.

3. Infrasound studies

As mentioned above, the smoke in the setup is sensitive to low-frequency acoustic pressure disturbances. As less than 1 μm of particle displacement is easy to discern with a high-magnification imaging objective, acoustic waves of this amplitude with frequencies below 15 Hz (one-half the frame rate) can be detected and analyzed. Assuming a particle excursion of ± 1.5 μm can be easily measured, a 1-Hz infrasound with an intensity of 51 dB (with reference to the 20-μPa 0-dB reference intensity) should be measurable with this setup, and lower intensities at lower frequencies.

IV. CONCLUSIONS

We have shown how a relatively simple and inexpensive smoke chamber and light-sheet experimental setup can be used to perform a variety of experiments pertaining to fluid dynamics, statistics, and electrostatics. We have shown quantitative agreement with theory for a Brownian-motion experiment and an experiment demonstrating the formation of long particle chains and suggested other experiments that can be performed with the same setup. The agglomeration of particles in outer space is currently an area of active research,[17] as it may play an important role in the early stages of planet formation. While conditions in these experiments differ from the vacuum of space, many of the principles are the same, making these experiments an interesting connection for students to current research.

ACKNOWLEDGMENTS

The author is grateful to the anonymous reviewers who provided extensive, careful, and constructive criticism of an earlier draft of this paper. The author thanks Brian Samuels for essential assistance with production of SEM images, Robert P. Cameron and Wolfgang Loeffler for helpful comments and suggestions, and Pamela Stephan for assistance with experiments. This work was partially supported by the Julian Schwinger Foundation under Grant No. JSF-16-04-0000.

AUTHOR DECLARATIONS

Conflict of Interest

The author has no conflicts to disclose.

[a]ORCID: 0000-0003-0967-3191.

[1]E. Wennstrom, "Development of a Brownian motion experiment for an undergraduate laboratory course," B.S. thesis (Oregon State University, Corvallis, OR, 2021).
[2]D. Germain, M. Leocmach, and T. Gibaud, "Differential dynamic microscopy to characterize Brownian motion and bacteria motility," Am. J. Phys. **84**(3), 202–210 (2016).
[3]M. J. Madsen and A. D. Skowronski, "Brownian motion of a trapped microsphere ion," Am. J. Phys. **82**(10), 934–940 (2014).
[4]J. M. Girkin and M. T. Carvalho, "The light-sheet microscopy revolution," J. Opt. **20**(5), 053002 (2018).
[5]H. S. Patterson, R. Whytlaw-Gray, and W. Cawood, "The structure and electrification of smoke particles," Proc. R. Soc. London, Ser. A **124**(795), 523–532 (1929). https://www.jstor.org/stable/95228

[6]A. R. C. Westwood and D. L. Goldheim, "Cleavage surface energy of {100} magnesium oxide," J. Appl. Phys. **34**(11), 3335–3339 (1963).
[7]M. A. Subramanian, R. D. Shannon, B. H. T. Chai, M. M. Abraham, and M. C. Wintersgill, "Dielectric constants of BeO, MgO, and CaO using the two-terminal method," Phys. Chem. Miner. **16**(8), 741–746 (1989).
[8]W. C. Hinds, *Aerosol Technology: Properties, Behavior, and Measurement of Airborne Particles*, 2nd ed. (Wiley, New York, NY, 1999).
[9]A. Einstein, "Über die von der molekularkinetischen Theorie der Wärme geforderte Bewegung von in ruhenden Flüssigkeiten suspendierten Teilchen (On the movement of particles suspended in liquids at rest, as required by the molecular-kinetic theory of heat)," Ann. Phys. **322**(8), 549–560 (1905).
[10]See supplementary material at https://www.scitation.org/doi/suppl/10.1119/5.0122766 for details of the data analysis of the Brownian-motion experiment and details of the general dynamic equation analysis of the long particle chain experiment, including analysis of the mutual electrostatic forces between chains.
[11]F. Poydenot *et al*., "Turbulent dispersion of breath by the wind," Am. J. Phys. **90**(11), 826–832 (2022).
[12]S. K. Friedlander, *Smoke, Dust, and Haze: Fundamentals of Aerosol Dynamics*, 2nd ed. (Oxford U. P., Oxford, 2000).
[13]A. Sugiura, M. Alexander, D. Knight, and K. Fujii, "Equivalent capacitance substitution method for monopole antenna calibration," in *2012 IEEE International Symposium on Electromagnetic Compatibility, Pittsburgh, PA* (IEEE, 2012), pp. 708–713.
[14]M. Smoluchowski, "Drei Vorträge über Diffusion, Brownsche Molekularbewegung und Koagulation von Kolloidteilchen (Three lectures on diffusion, Brownian motion, and coagulation of colloidal particles)," Phys. Z. **17**, 557–585 (1916). https://hdl.handle.net/2027/mdp.39015010783705
[15]G. K. Batchelor, *An Introduction to Fluid Dynamics* (Cambridge U. P., Cambridge, 1967).
[16]N. A. Fuchs, *The Mechanics of Aerosols* (Pergamon, New York, 1964).
[17]C. Dominik, J. Blum, J. N. Cuzzi, and G. Wurm, "Growth of dust as the initial step toward planet formation," in *Protostars and Planets V* (University of Arizona, Tucson, AZ, 2006).

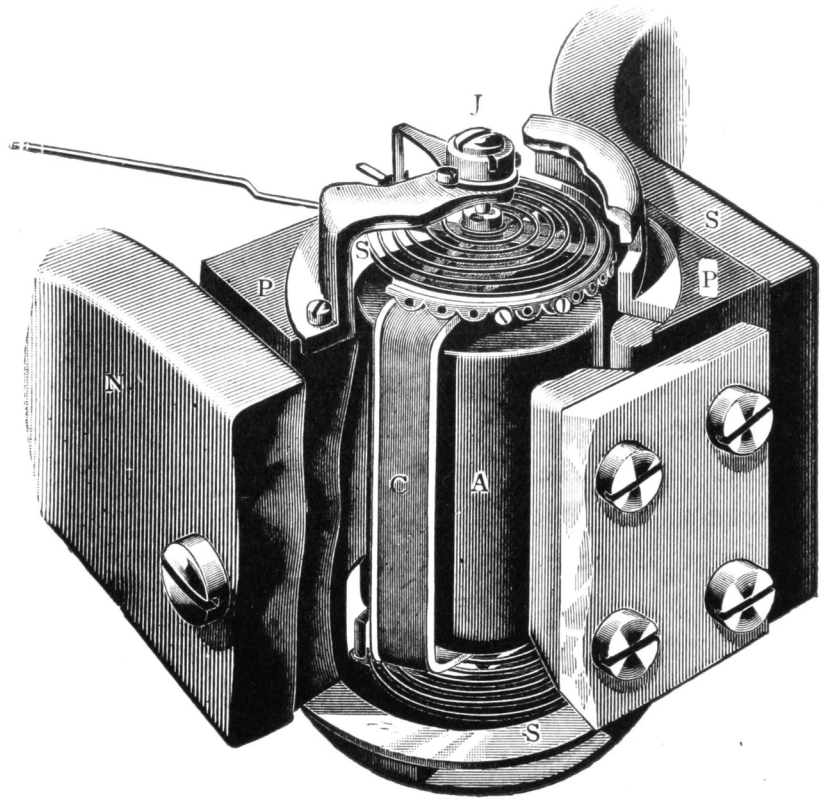

Edward Weston's Galvanometer Movement.

Edward Weston announced his design for a portable meter movement in 1884. He used jeweled pivots to support the coil, and non-magnetic helical springs to provide the restoring torque. The pointer was made of flattened slender aluminum tubing to reduce its moment of inertia, and the coil was wound on a light copper form. Eddy currents in the copper provided the damping that kept the needle from oscillating. The magnetic pole faces were circular, and the coil moved in the narrow gap between the faces and a soft iron cylinder placed concentric to the pivot of the coil. The magnetic field lines were always radial, which ensured that the plane of the coil was always perpendicular to the magnetic field lines, producing a linear scale. Weston developed a method of ageing the permanent magnets so that their field remained steady. The figure is from a 1904 treatise on electricity. (Picture and text by Thomas B. Greenslade, Jr., Kenyon College)